# Synchrotron radiation based dark-field lung imaging: an analyzer-free dual-phase approach for radiography and CT

**Simon Spindler[1,2,*], Alexandre Pereira[1,2], Caori Organista[1,2], Marie-Christine Zdora[1,2], Goran Lovric[2], Ginevra Lautizi[3,4], Christian Dullin[5], Adriano Contillo[3], Elena Longo[3], Nicola Sodini[3], Lorenzo D'Amico[3,4], Lucia Romano[1,2], Konstantins Jefimovs[2], Daniel Josell[6], Michał Rawlik[1,2], Giuliana Tromba[3], and Marco Stampanoni[1,2]**

[1]Institute for Biomedical Engineering, ETH Zurich, Switzerland
[2]Center for Photon Science, Paul Scherrer Institute, Switzerland
[3]Elettra-Sincrotrone Trieste S. C. p. A., Basovizza, Trieste, Italy
[4]Department of Physics, University of Trieste, Trieste, Italy
[5]Department for Diagnostic and Interventional Radiology, University of Goettingen, Germany
[6]Materials Science and Engineering Division, NIST, USA
[*]simon.spindler@psi.ch

## ABSTRACT

Lung diseases such as chronic obstructive pulmonary disease are a major health burden to society for which early detection plays a crucial role for treatment success. For detection, as well as diagnosis and serial evaluation, imaging plays a major role, but lung diseases are often still diagnosed in progressed states for which effective causal therapies do not presently exist. Recently, dark-field lung imaging has been introduced as a promising technique for early stage detection of alterations in lung micro-structures. This work presents an analyzer-free, full-scale lung imaging system based on a dual-phase interferometer, which allows tuning and direct resolution of grating induced intensity fringes. It provides the classical absorption chest image with additional dark-field information without significant attenuation of the patient-exposed photon-flux or the cost of large area absorption gratings. The detailed system achieves a dark-field sensitivity adequate for lung imaging, governed by system autocorrelation lengths of up to 0.6 µm. The computed tomography (CT) reconstructions show further evidence of the emergence of the dark-field in the parenchyma.

## Introduction

Chronic respiratory diseases affect roughly every thousandth person globally [1,2] causing millions of deaths each year. A particular problem is the slow, gradual progression of irreversible damage in the lung micro-structure (emphysema or fibrosis), which is often diagnosed only after the first symptoms appear. At this point, treatment is already difficult as only the symptoms but not the root-cause can be treated. In recent years, there have been notable advances in the field of lung imaging ranging from high-resolution synchrotron imaging of small murine lungs [3–5], human-scale lung imaging with porcine lungs at synchrotrons [6,7] to human dark-field lung imaging in hospitals [8,9], but a diagnostic tool sensitive enough to detect these gradual changes before symptoms arise remains highly needed.

The penetrating nature of X-rays allows for partial propagation through objects, yielding both a change in intensity and direction. This allows imaging in a non-destructive manner that is widely used in medical and industrial applications [8,10–12]. Most of these applications utilize only the attenuation of X-rays by the samples. The most sensitive attenuation-based diagnostic tool to detect early forms of emphysema or fibrosis in the lungs is chest CT. Although CTs are capable of measuring changes in the attenuation properties, the applied dose is high for screening applications [13] (typically above 1 mGy [14]). With the use of coherent X-rays it has become possible to routinely sense also the refractive properties of objects. Synchrotron facilities leverage high spatial and temporal coherence to allow direct detection of the interference generated by objects (e.g., edge enhancement) [15].

Grating interferometers utilize the Talbot effect to generate intensity fringes that can be measured on table-top X-ray sources, which lack the spatial coherence of synchrotrons, using appropriate grating configurations and at much larger pixel sizes [16]. The gratings generate spatial coherence (source grating), induce intensity fringes (diffraction grating), and/or analyze

the fringe structure (analyzer grating). The analyzer grating is necessary to sample fringe periods smaller than the pixel size through phase-stepping or fringe scanning [16,17]. An advantage of grating interferometers, is that they measure the geometric refraction of an object. This allows tracking of scattering/diffusion that leads to a reduced intensity difference between the high and low intensity regions of the fringe.

The diffusion property, captured in the dark-field, is caused by diffuse refraction of unresolved (micro-) structures or sharp edges [18] and is difficult to obtain with direct imaging approaches. The dark-field signal obtained from an interferometer is dependent on the autocorrelation length [19] $\xi$ of the system defined as:

$$\xi = \frac{\lambda L}{p_f}, \tag{1}$$

where $\lambda$ is the wavelength, $L$ the sample-to-detector distance and $p_f$ the period of the fringe. The blurring of the fringe is maximal when the autocorrelation length and the micro-structure sizes are approximately equal [20,21]. Strong diffusers can blur the fringe enough for it to become indistinguishable from noise, leading to a uniform illumination and rendering the dark-field signal as a lower bound for the actual signal [22].

In the context of lung imaging, dark-field lung radiography is a promising option for screening programs due to its sensitivity to the micro-structures even at low doses, which would enable the tracking of lung micro-structure over time; lungs generate a strong dark-field signal due to the large difference of the refractive indexes of air and tissue. To be sensitive to small variations in the dark-field, and thereby the structure size, unsaturated signals are necessary. Lung imaging thus requires autocorrelation lengths orders of magnitude smaller than the alveolar structure size of roughly 200 µm [22] in order to not saturate through 20 cm of lung tissue.

Dark-field lung imaging devices [8,9,23] are typically three-grating systems consisting of a source grating, diffraction grating and analyzer grating. Most grating interferometers are designed for a specific configuration, inducing a well-defined energy and fringe periodicity. This leaves only the sample-to-detector distance as a parameter to change the autocorrelation length, resulting in a concurrent variation of the sample magnification in the case of a divergent beam geometry, complicating the dark-field analysis of the identical region of the sample.

Dual-phase interferometers, as used for this study, generate Moiré-fringes of tunable period by superimposing the Talbot carpets from two phase gratings [24–26], providing more freedom for scanning the autocorrelation length space. The Moiré-fringe spacing can be varied by changing the distance between the two gratings. This has two significant advantages: the fringe spacing can be made large enough for the fringe to be resolved directly with the detector and the autocorrelation length can be tuned without moving the sample. Further, the method provides a reproducible dark-field analysis of the same structures for all the autocorrelation lengths.

Resolving the fringe directly is advantageous as absorption gratings reduce the radiation exposed to a patient and worsen the image quality. The radiation dose is directly related to the number of counts that can be measured on a detector and, with it, image noise. Absorption gratings are problematic when placed after a patient as they yield worse images for the same applied radiation dose. Therefore, analyzer gratings reduce the dose efficiency of an imaging system compared to devices without them. The differential phase contrast and dark field should outweigh the increased noise to obtain diagnostic value. Absorption gratings are also expensive, difficult to manufacture and, for insufficiently large gratings, need to be stitched together with complex mechanical fixtures.

In this study the feasibility of dark-field lung imaging without analyzer gratings is evaluated at the SYnchrotron Radiation for MEdical Physics (SYRMEP) beamline at Elettra. Analyzer-free systems are challenging to build for the autocorrelation lengths needed in dark-field lung imaging due to the large fringe periods required for the pixel sizes of commercially available X-ray detectors. The SYRMEP beamline provides infrastructure enabling autocorrelation lengths between 0.2 µm and 0.8 µm, relevant for clinical dark-field lung imaging, for which no autocorrelation length-dependent dark-field scan has been published to date. As porcine lungs have been used as a stand-in for human lungs in many translational medicine studies [27], this study uses a lung phantom to scan inflated porcine lungs under conditions enabling dark-field radiography and CT close to clinical conditions. The dark-field images obtained show the system's sensitivity to lung micro-structures. The results demonstrate the feasibility of dual-phase imaging with synchrotron radiation, measuring the dark-field signal of porcine lungs over a previously unreported autocorrelation length range and suggesting a system design tailored to image human lungs in radiography.

## Methods

### SYRMEP Beamline and Sample Preparation

The experiments were conducted at the SYRMEP imaging beamline of the ELETTRA synchrotron facility in Trieste [28], Italy. The 3rd-generation storage ring, of 259 m circumference, was operated in top-up mode [29] at an electron energy of

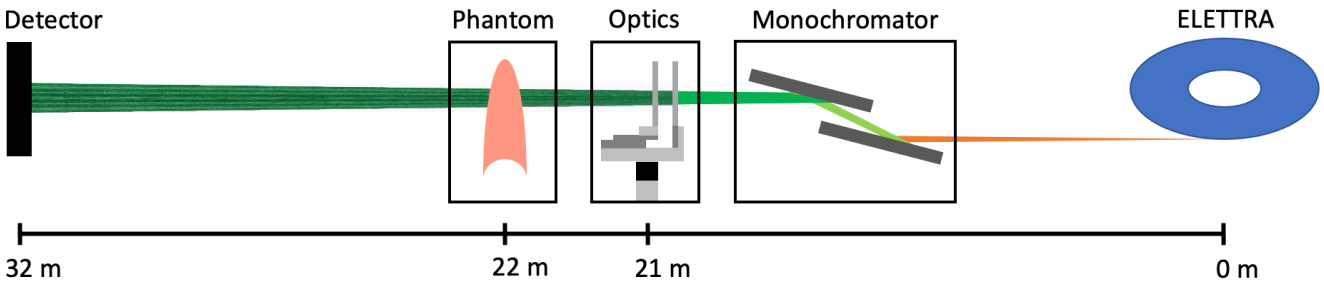


**Figure 1.** A schematic drawing of the experimental setup used at the SYRMEP beamline. The experiment utilized 40.8 keV monochromatic radiation, and the dual-phase grating optics were placed 21 m from the source, with the lung phantom at 22 m and the detector at 32 m.

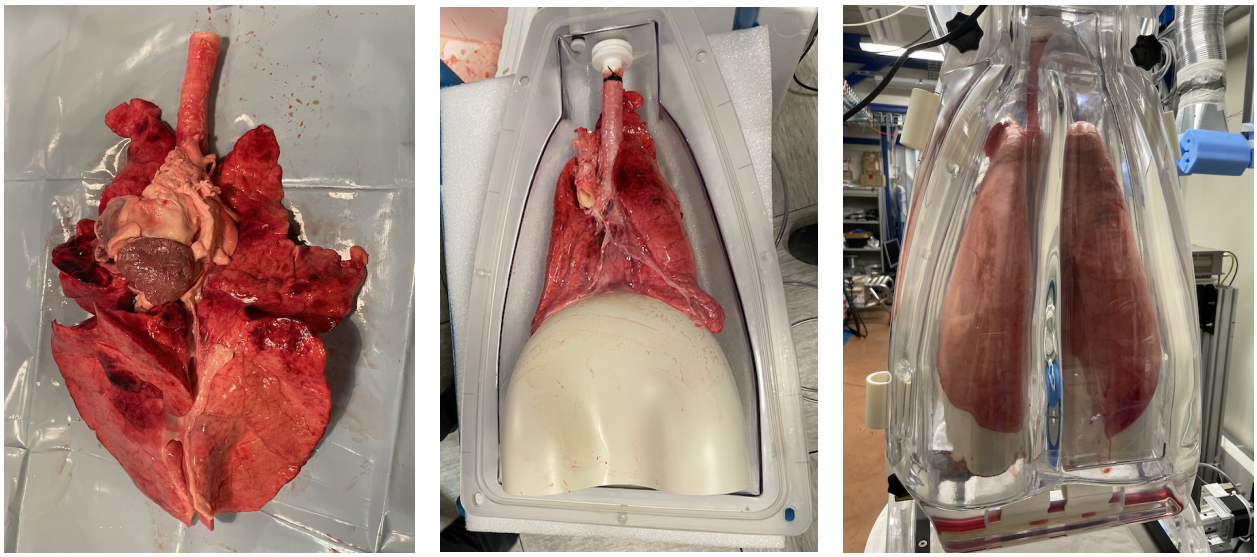

**Figure 2.** Preparation and mounting of porcine lungs into the phantom. *Left:* The outer membrane and most of the surrounding fat tissue were removed from the lungs, leaving the heart muscle. Cuts were sewn or glued shut to ensure proper inflation of the lungs. *Middle:* The prepared lungs were placed in the phantom onto a loosely placed artificial diaphragm, supporting the weight of the lungs from beneath to minimize the force on the trachea, which is tied to the air inlet. *Right:* The same inflated porcine lungs installed on the sample stage inside the experimental hutch.

2.4 GeV with a ring current of 150 mA. As sketched in Fig. 1 the SYRMEP beamline has a bending-magnet source of 1.45 T, a monochromator providing well-defined energies with a specified energy range between ~~from~~ 9 keV to 40 keV [30] with a beam size of $120 \times 4\,\mathrm{mm}^2$, at the sample position as well as a series of aluminum filters to suppress lower harmonics from the monochromator or to reduce the flux in general (a 7.5 mm filter was used). The experimental hutch is located 21 m downstream of the bending magnet and allows system configurations up to 32 m from the source spot, which is specified to be 327 µm wide (full width at half maximum (FWHM)) [31]. For the experiments a photon-counting CdTe XCounter (XC Hydra) detector with $2064 \times 62$ pixels, 100 µm on a side, was used in charge-integrating mode with a threshold set to 20 keV to count all radiation above this value.

The SYRMEP beamline offers an anthropomorphic chest phantom [7] that permits inflated porcine lungs to be imaged as seen in Fig. 2. The lungs are inflated by applying a constant negative pressure to the chamber of the thoracic phantom with the trachea at ambient pressure; this allows the lungs to draw air in a manner similar to that during physiological breathing. As lung tissue needs to be elastic in order to be inflated properly, the lung samples were frozen to keep them fresh/elastic and slowly defrosted in a styrofoam box over 5 to 6 hours before placing them in the phantom. To mount the lungs in the phantom, the lungs were cleaned, trimmed of excess tissue and checked for cuts or other damage which was sealed as necessary. They were subsequentially placed in the pressure container, with the trachea connected to the air inlet, supported on a diaphragm. The phantom was placed on a sample stage [32] in the beamline hutch for the acquisition of radiography and CT scans.

## Dual-Phase Interferometry

There are different types of interferometry systems, each with its own advantages and disadvantages. Talbot-Lau interferometers are widely used and have been studied extensively leading to well understood analysis protocols; however, they generally lack flexibility after the design process as they are fixed to a single fringe period. For the experiments in this work, a dual-phase system [24] was chosen for its ability to provide variable fringe sizes.

The dual-phase interferometer consists of two phase gratings, each inducing intensity fringes through the Talbot effect downstream. The superposition of carpets of different period, due to gratings of different pitch and/or propagation-based magnification between the spaced gratings, generates Moiré-fringe patterns. These Moiré-fringes can exhibit a wide range of periods $p_f$, which allows for measurement at various autocorrelation lengths without moving the sample from its fixed location, in accord with Eq. 1. With two gratings of equal period the fringe period $p_f$ is [25]:

$$p_f = \frac{sp}{2d_g}, \tag{2}$$

where $s$ is the total system length, $p$ ($=p_1=p_2$) is the period of the phase gratings and $d_g$ is the distance between the two phase gratings.

The source size required to obtain high visibilities can be calculated by considering a displacement of a second source horizontally and perpendicular both to the beam axis and the grating lines to obtain the same fringe. This is analogous to the period $p_0$ of a source grating at the source's position [25]

$$p_0 = \frac{p_f p_1 p_2}{2p_f(p_2 - p_1) + p_1 p_2}. \tag{3}$$

Increasing the size of the transmission lines (sources) will lead to an increased duty cycle of the grating, reducing the visibility of the fringe. This shows that the source size is ideally below 50 % of $p_0$ to obtain desired visibilities. This consideration is just a way to calculate the source size, no source grating was used in the system.

For this experiment a dual-phase grating holder was built to optimize the grating alignment procedure and allow for a wider range of distances between the gratings. The design is shown in Fig. 3 and consists of three piezo-positioner motors (SmarACT, Germany) as well as one manual goniometer (OptoSigma, USA). One phase grating is mounted on a linear piezo-drive oriented perpendicular to the beam axis (Fig. 3 *A*) for the phase-stepping measurements. The second phase grating is mounted on a second linear piezo-drive (Fig. 3 *B*) that permits the distance between the two gratings to be changed. The distance of the beamline hutch to the source point results in only a small magnification between the two gratings, so a long travel range (upwards of 6 cm) is required for the gratings to generate fringe sizes on the order of a few hundred micrometers. The long motor (*B* in Fig. 3) of the grating holder provides a movement range of 10 cm, which allows for generation of fringes from well above 1 mm down to below 100 µm (the resolution capabilities of the detector), as can be determined through analytical calculation (Eq. 2) [25] or numerical wave propagation calculations [33–35]. On linear drive *B*, a piezo-goniometer (Fig. 3 *C*) permits alignment of the grating structures (i.e., trenches) of the two gratings. The whole motorized part is mounted on a manual goniometer (Fig. 3 *D*) which allows for tilting of the aligned dual-phase fringe relative to the detector. This design covers the necessary degrees of freedom, allowing for a reliable and simple alignment of the gratings.

The data were acquired with a monochromatic 40.8 keV dual-phase system consisting of two 1 µm-pitch phase gratings [12] and autocorrelation lengths ranging from 0.29 µm to 0.67 µm. The gratings used for the experiments were patterned with 9.2 µm deep trenches at a 1 µm pitch and 50:50 duty cycle, etched into silicon (100 mm diameter and 250 µm thick double side polished wafers) by deep reactive ion etching [36] and filled with gold [12], providing a $\pi$-shift at 40.8 keV. Notably, no X-ray optics were placed behind the lungs.

## Image Analysis

Dual-phase interferometers have a complex fringe profile [37]. This is evident in the non-sinusoidal shape of the phase-stepping curve shown in Fig. 4, which illustrates the intensity measured at a single pixel as the trenches in one phase grating are shifted in the plane of the grating, orthogonal to the trenches in the other grating, over/along the distance of the trench pitch. Unlike the single frequency sine wave often assumed for Talbot-Lau interferometers, the general dual-phase fringe or phase-stepping curve is modeled with two frequency components, necessitating more phase steps to resolve the two phases. For the experiments in this work the results were fitted to two superimposed sine curves, one at, and one double, the visible fringe frequency [38]:

$$I(x) = A\left(1 + V_1 \sin\left(\frac{2\pi x}{n} + \phi_1\right) + V_2 \sin\left(\frac{4\pi x}{n} + \phi_2\right)\right), \tag{4}$$

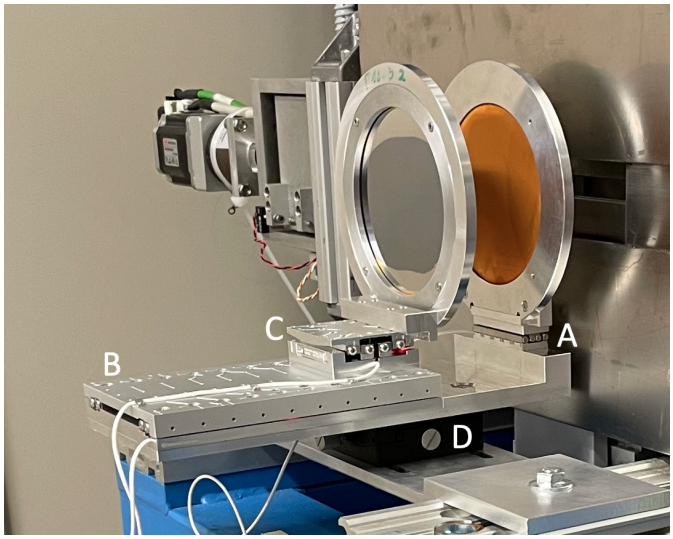


**Figure 3.** Image of the dual-phase grating holder installed at the beam entry into the SYRMEP experimental hutch. It consists of piezo motors for phase-stepping (A), changing the inter-grating distance (B) and making the grating lamellae parallel (C), as well as a manual goniometer to align the fringe to the detector (D).

where $I(x)$ is the pixel intensity at the phase step $x$ of $n$ phase steps for a full period, $A$ is the intensity, and $V_1$ ($V_2$) is the visibility of the first (second) frequency with the phase offset $\phi_1$ ($\phi_2$). The term $\phi_2$ is the offset of the second frequency term and is not shifted relative to $\phi_1$ at different locations on the sample (i.e., $\phi_2 = \phi_1 + \Delta$, where $\Delta$ is a phase offset between the two sine terms in Eq. 4). In order to fit both frequency components, 15 to 20 phase steps were performed over a grating period. To analyze the data, a flat-field phase-stepping curve, Eq. 4, was fitted for every single pixel, obtaining all constant parameters (the number $n$ of steps required for a period and the relative displacement of phase $\phi_2$ from phase $\phi_1$), which were inserted in all further fits making the signal retrieval more efficient and accurate.

Both the attenuation and dark-field follow the Beer-Lambert law, which describes an exponential decrease of the corresponding parameter (intensity for attenuation and visibility for the dark field, respectively). The dark-field extinction coefficient (similar to attenuation coefficient but describing the amount of diffusion per thickness) can also be obtained if the thickness of the imaged object is known.

The attenuation $\Lambda$ is calculated by

$$\Lambda = -\ln\left(\frac{A_s}{A_{ref}}\right), \tag{5}$$

where $A_s$ is the overall image intensity with the sample in the beam and $A_{ref}$ is the intensity of the reference image without the sample. The overall dark-field $\Sigma$ is defined as

$$\Sigma = -\ln\left(\frac{V_s}{V_{ref}}\right), \tag{6}$$

and gives the reduction of the linear combination of both visibilities $V = V_1 + V_2$, where $V_s$ and $V_{ref}$ are the visibilities of the sample and reference measurement, respectively. An interesting quantity to consider is the so-called $R$ value [39], defined as:

$$R = \frac{\Sigma}{\Lambda}, \tag{7}$$

which is a thickness-normalization of the dark-field of a homogeneously diffusing sample and thus gives insight into the mean diffusion coefficient. For dark-field lung imaging this value can give information about lung regions with higher and lower scattering properties, i.e., regions with smaller or larger overall feature sizes or volume fractions, and is potentially important for the diagnosis of diseases like chronic obstructive pulmonary disease [40]. The differential phase contrast is defined as $\mathrm{dpc} = \phi_{1_{sample}} - \phi_{1_{ref}}$ ~~erence~~ with $\phi_1$ being the phase shift from Eq. 4.

As each image sampled a vertical field of view (FOV) (i.e., height along the area of specimen) of $\approx 2$ mm, the radiography images were stitched from projections at different sample heights, taking the mean within the overlapping regions.

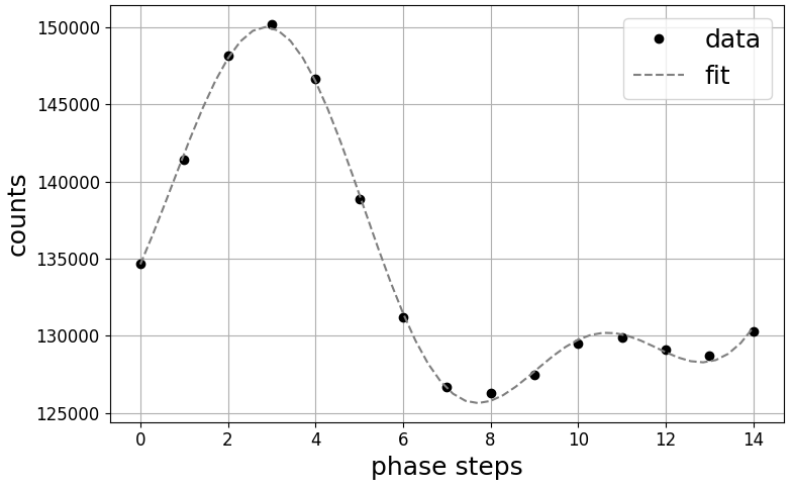


**Figure 4.** A phase-stepping measurement of 15 steps over a 1 µm period fit to Eq. 4 at a single measurement position. The shallower the oscillation in the fringe, the lower the value of visibility.

For the CT reconstructions a filtered back-projection algorithm of the ASTRA toolbox [41,42] for parallel beam geometry was performed. The images of the projections at each angle were flat-field corrected and re-arranged into sinograms and reconstructed separately in attenuation and dark-field.

## Results

Results from the system characterization followed by dark-field imaging of porcine lungs without analyzer gratings under radiographic and CT acquisition settings are now presented.

### System Characterization

To characterize the dual-phase interferometer, the full available inter-grating distance was scanned to match motor positions to fringe sizes observed at a single location (as in Fig. 5). For fringe periods between 1100 µm to 500 µm phase-stepping measurements with 15 to 20 phase steps were performed as shown in Fig. 4, displacing one phase grating over its 1 µm period to evaluate the linear combination of the $V_1$ and $V_2$ visibility values for the autocorrelation lengths of all configurations (per Eq. 1), as shown by the black data points in Fig. 6. The overall autocorrelation length range for this system was between 0.29 µm and 0.67 µm, however, the larger autocorrelation lengths had lower fringe visibility. Fig. 6 shows that the visibility curve can be recreated for a source size of (500 ±50) µm, compared to a stated nominal horizontal source size of 327 µm at SYRMEP by Peiffer *et al.* [31]. The monochromatic 40.8 keV wave propagation simulations from the RaveSim package [35] in Fig. 7 that predict these visibility values also show that, with increasing source size, the visibility reduces more rapidly for smaller fringes. The entrance dose-rate of the imaging setup was 0.56 mGy per second, measured with a thermo-luminescence dosimeter of 4.5 mm diameter (GR-200 A, based on LiF:Mg,Cu,P; Hangzhou Freq-control Electronics Technology Co., Ltd) and compared to measurements of an ionization chamber.

### Radiography

To benchmark the dark-field lung imaging capabilities of the system, polymethylmethacrylate (PMMA) micro-spheres (Cospheric LLC, USA) were utilized due to the scattering properties broadly resembling those of lung tissue [22,43]. In order to compare the R-value of lungs and PMMA spheres, the attenuation was adjusted to account for the inverted spatial filling of the diffusing structures [22] (PMMA spheres are filled spheres surrounded by air, where lungs are air spaces surrounded by tissue). Three vials with 1 cm diameter were filled with PMMA spheres of different size in the range of: 20 µm to 27 µm, 180 µm to 212 µm and 425 µm to 500 µm. The average dark-field signal corresponding to each autocorrelation length can be seen in Fig. 8. The PMMA spheres were imaged with 45 phase steps and an exposure time of 3 s per phase step.

The inflated porcine lungs, prepared as shown in Fig. 2, were also imaged. Due to the phantom's significant attenuation, with Λ values exceeding 5 and thus much higher than the lungs themselves, the measurements were adjusted for the phantom's attenuation using data from an empty phantom measurement. The R-values for the lungs are shown along with the PMMA values in Fig. 8. The image of a full lung lobe shown in Fig. 9 (and Fig. S1) includes 120 vertical images stitched together, each obtained with 3 s exposure time at each of the 15 phase steps, requiring a 1.5 h total acquisition time.

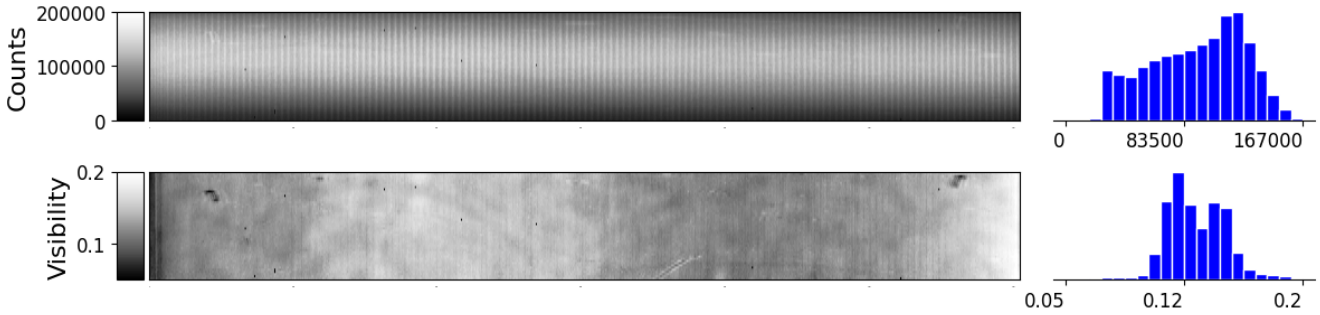


**Figure 5.** Images of the fringe with a period of 800 µm. To the right of the images the histogram is displayed. Top: The raw fringe image with the spatial variation of counts according to the gray-scale shown on the left. Bottom: Map of the assessed visibility with the local value according to the gray-scale shown on the left.

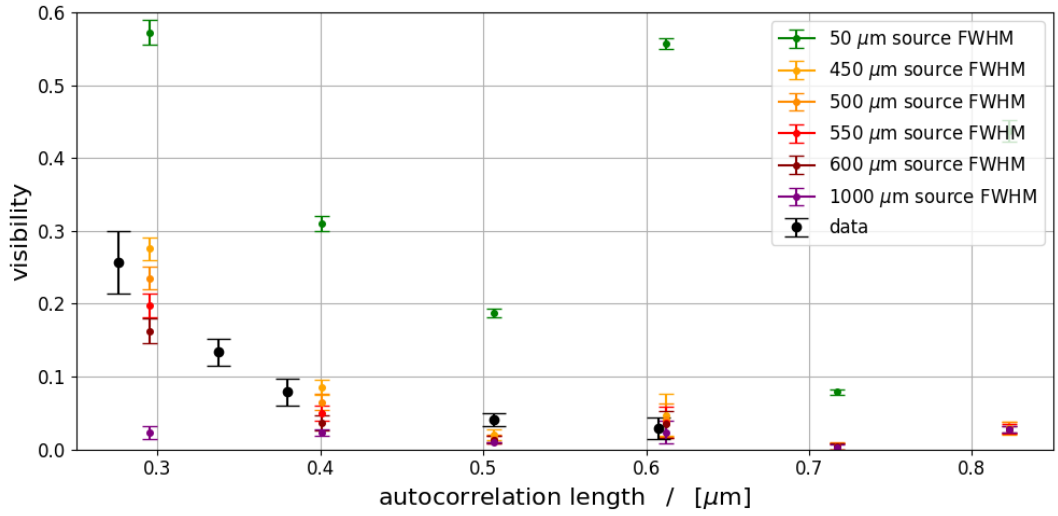


**Figure 6.** The mean visibility plotted over the autocorrelation lengths of the measurement points with an exponential fit in black. Simulated Gaussian source sizes show a reduction in visibility with increasing source size. Comparison of the data and simulations indicates a full width at half maximum (FWHM) of the source size at SYRMEP between 450 µm and 550 µm. The data points correspond to the mean value of the measured and simulated visibilities, and the error-bars are the standard deviation of the distributions.

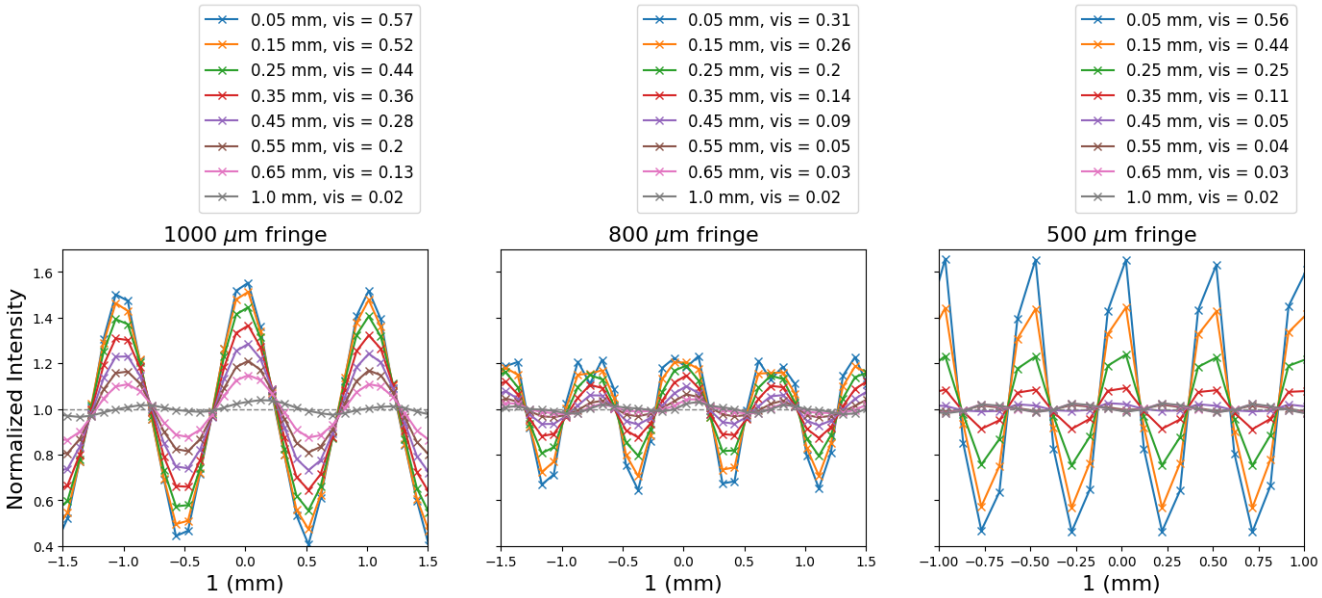


**Figure 7.** Simulations of the fringes for different source sizes and the indicated values of system visibility (vis). *Left:* Simulation for a fringe size of 1000 µm. *Middle:* Simulation for a fringe size of 800 µm. *Right:* Simulation for a fringe size of 500 µm. With decreasing fringe size, the source size penalty increases as expected from Eq. 3. The fringes show examples from which the visibility simulation points from Fig. 6 were obtained.

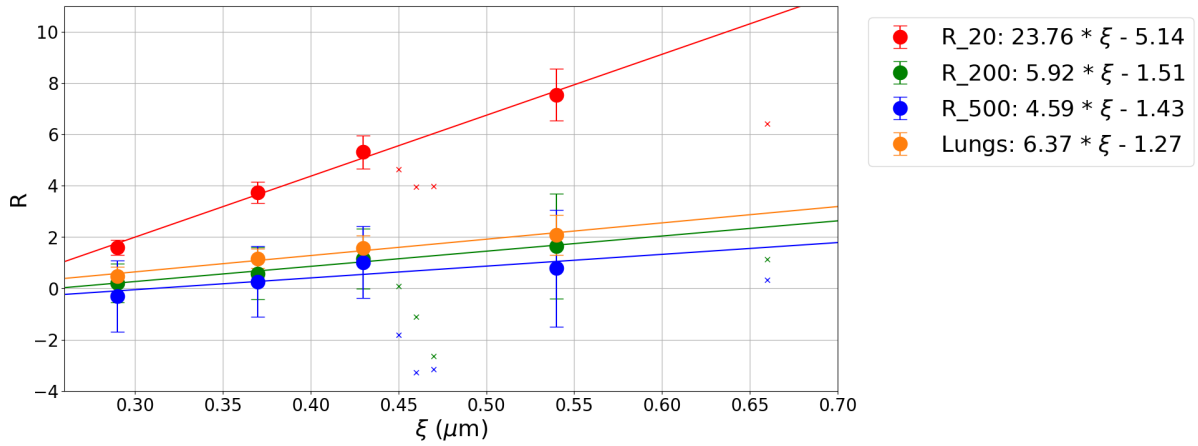


**Figure 8.** A scatter plot of the measured R-values (scaled combined visibility normalized by scaled attenuation as per Eq. 6) for the three sizes of PMMA spheres and the porcine lung acquired for the select motor positions with a linear fit to the data for each. The absorption data for the PMMA spheres were adjusted with a factor of 1.778 [22] to account for the inverse filling of the space. The x-markers are measurements that were excluded from the analysis due to problems with the diffraction orders close to the fringe period (vide infra, Fig. S2) and insufficient visibility (at the highest autocorrelation lengths). The points correspond to the mean values of a region of interest, while the error bars correspond to the standard deviation of the region of interest.

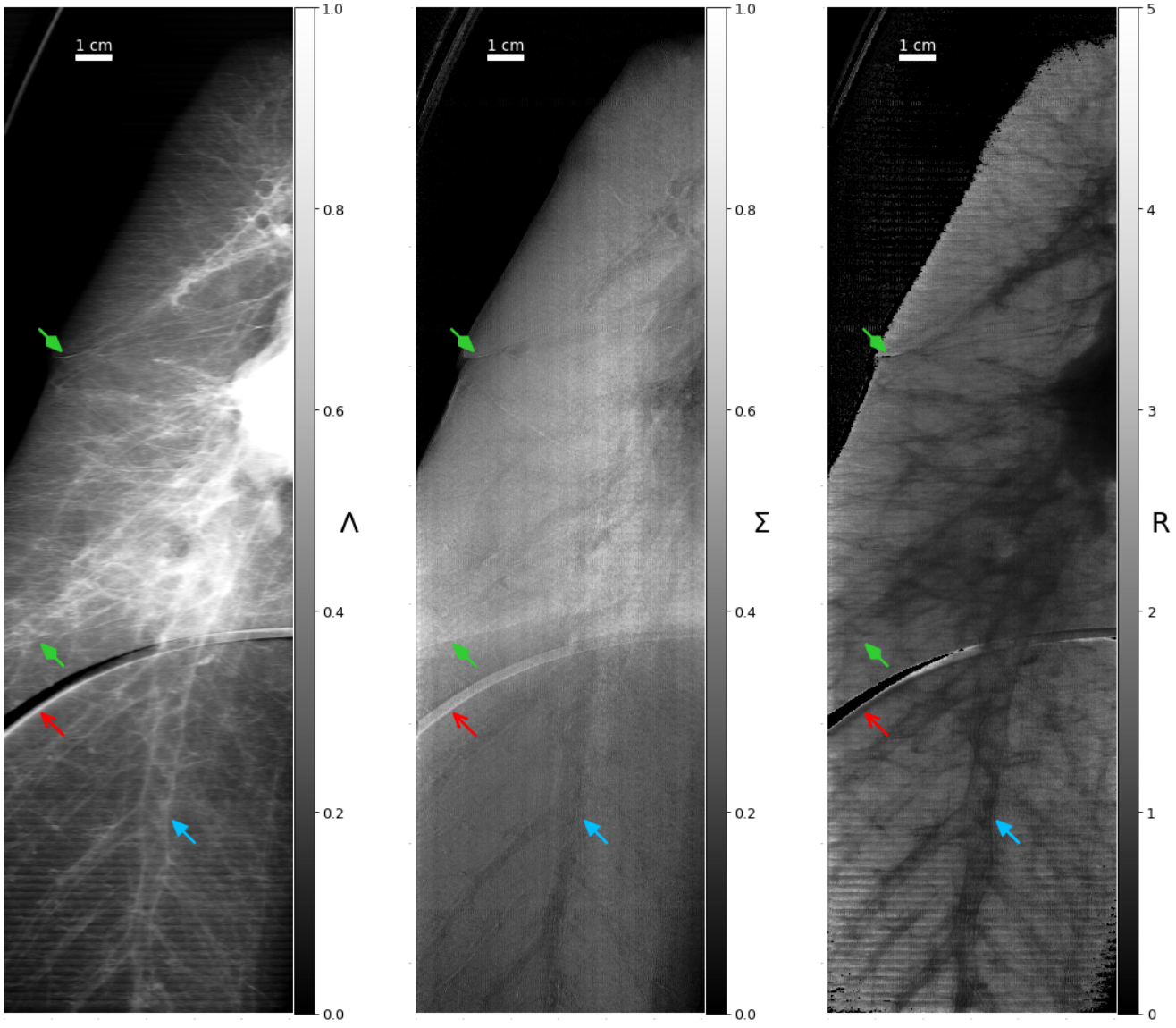


**Figure 9.** Stitched planar views of an inflated porcine lung at an autocorrelation length of 0.36 µm. The images consist of 120 fields of view, each 2 mm tall (vertical) and acquired in 45 s with 15 phase steps, for a total acquisition time of 1.5 h. *Left:* The attenuation image was corrected for the container attenuation. *Middle:* The dark-field channel. *Right:* The R-value. The forked red arrows point to artifacts from the artificial diaphragm. The triangular blue arrows point out one of the visible bronchi. The green diamond head arrows highlight interfaces (lung fissures) between different lobes of the lung.

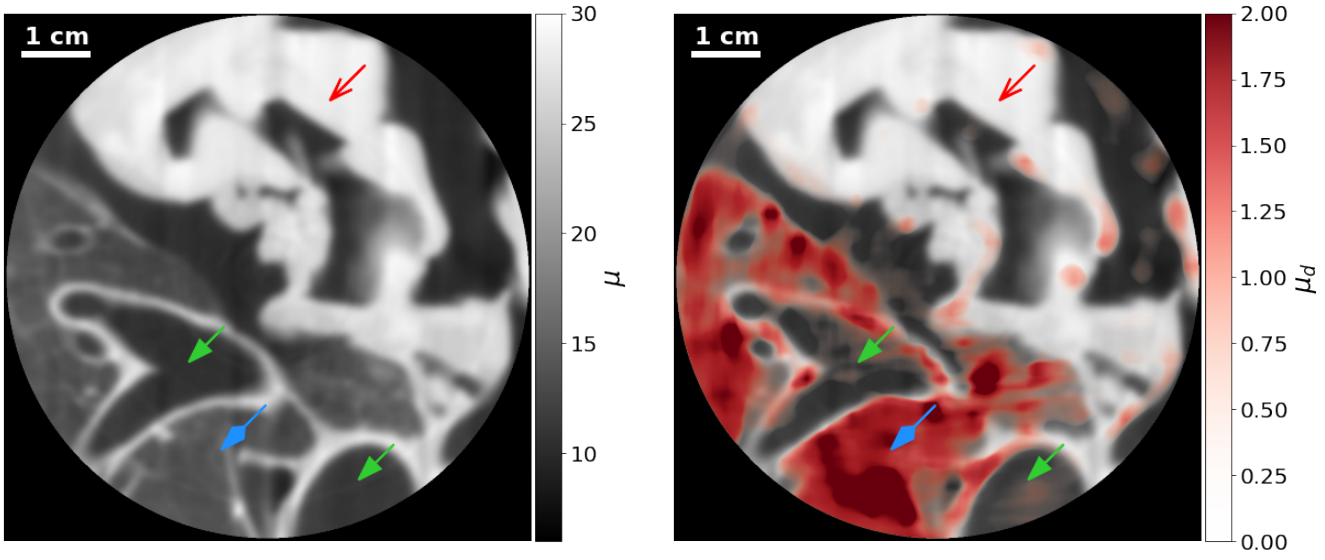


**Figure 10.** CT reconstructed slice of a porcine lung. The green arrows with triangular heads point to air spaces (secondary bronchi), the red arrow with forked head points to heart tissue and the blue arrow with diamond head to lung tissue. *Left:* The attenuation image of the lung, with gray scale bar to the right. *Right:* The median filtered extinction coefficient is superimposed on the attenuation image with extinction coefficients close to 0 being transparent and the higher coefficients having deeper red coloring according to the scale bar to the right. Lung tissue causes diffusion while the large air cavities as well as the heart tissue without micro-structures do not.

### CT

Tomography scans, shown in Fig. 10, were acquired for a region of the lungs. The acquisition involved a full tomographic scan for each phase step, a single phase step taking 5 min for 3000 projections over 180 ° of sample rotation, adjusted for the visibility at the autocorrelation length of 0.36 µm. The total acquisition of the dark-field CT took 100 min for the tomographic scan (20 phase steps times 5 min). The CTs were binned by a factor of 250 (2 horizontal by 25 vertical pixels over 5 angular projections, binned to a single value) due to the low fringe visibility and strong absorption of the phantom, which reduced the overall counts. To obtain an unsaturated [22] signal in the retrieved sinogram for the dark-field, the raw data were binned over the full vertical FOV and 5 projections in the angular direction (in total 0.18 ° per frame). This led to unsaturated data for even the thickest and most diffusing regions in the sinogram.

The container also caused phase-wrapping artifacts, interfering with signal retrieval according to Eq 4. Technical issues with the rotation stage also resulted in missing projections that created streak artifacts in the reconstructed dark-field tomograms. A Fourier wavelet filter [44] was applied on the sinograms to remove ring artifacts. The results were additionally filtered by a gaussian filter of kernel size 6 to remove the diffraction order effects.

To superimpose the dark-field data on the attenuation reconstruction, a linear color-bar was generated which is transparent at zero and fully opaque red at a set threshold. The dark-field reconstruction was superimposed on the attenuation reconstruction to produce the right image in Fig. 10.

### System Optimization

The interferometer presented was constructed using available hardware and gratings, and optimized for the existing beamline. A custom design would enhance the system's performance by addressing its limitations. Specifically, as shown in Eq. 3, increasing the period of the phase gratings not only allows lower Talbot order systems to improve visibility but also reduces source size constraints. Additionally, rotating the gratings by 90 ° could utilize the smaller source size in the beam's vertical direction. For a system targeting an autocorrelation length of 0.36 µm, the optimal configuration would involve 2.2 µm phase gratings, yielding predicted visibilities close to 30 %. The planned upgrade of ELETTRA 2.0 [28,45] will also reduce the source size, thereby improving visibility.

## Discussion

This study demonstrates the feasibility of dark-field imaging without analyzer gratings at a synchrotron imaging beamline, providing classical attenuation images as well as dark-field data compared to conventional X-ray imaging setups that provide

only the former. The method is demonstrated using human-relevant porcine lungs with radiograms of the attenuation and dark-field contrasts as well as a CT reconstruction.

Dual-phase interferometry is a versatile system for assessing the dark-field properties of a sample over the autocorrelation length space because the sample does not have to be moved. For systems with polychromatic sources this does, however, lead to the need for beam hardening corrections as changing the fringe period also changes the spectral properties of the system [46]. For monochromatic sources as used here, such correction is not necessary. The dual-phase fringe is not a simple sinusoidal curve [26,37] and varies throughout the image. As captured in Fig. 4, the model introduced in Eq. 4 fits the data well. Although more phase steps are necessary to fit the two frequency components, phase-stepping provides a more reliable signal retrieval than single shot fringe analysis.

The results in Fig. 8 show R-values and trends with autocorrelation length for the PMMA micro-spheres and the lungs as were obtained in an earlier study on a polychromatic Talbot-Lau interferometer [22]. The lungs in this study induced a dark-field signal more closely resembling densely packed 200 µm diameter PMMA spheres compared to the previously reported values [22]. This is likely due to higher differential pressure between lung and ambient that caused the alveoli to expand more and leading to a lower dark-field signal. Also, the overall slope of the dark-field or R-value over the autocorrelation lengths (provided in Fig. 8) is larger compared to the study [22], which can be attributed to visibility hardening [47] that is manifest in the gradual reduction of the slope towards saturation under their polychromatic illumination. The radiographs in Fig. 9 show the added information provided by the dark-field. This includes signal generated by the alveoli, the measurement being sensitive to the mean structure size [19–21], and could benefit the diagnosis of emphysema, fibrosis or similar diseases that alter the structure of the lung and are hence expected to change the dark-field signal [48]. The R-value of the radiography is constant for the lung tissue and drops for regions with large air vessels which have relatively thick and absorbing walls. This is also evidence for a uniformly inflated lung without noticeable tissue damage from slaughter process, freezing or disease. The artifact visible in the middle region of Fig. 9 (and Fig. S1) stems from the diaphragm underneath the lungs (visible in Fig. 2 on the middle image) which is not fixed to the outer shell of the phantom and is moved between the sample and reference measurements.

The attenuation images of the PMMA micro-sphere containers showed diffraction artifacts as visible in Fig. S2. We thoroughly investigated this issue and have provided detailed findings in the supplementary materials. Despite our understanding of these artifacts (Fig. S3 and Fig. S4), we were only able to partially mitigate and correct them.

The dark-field of dual-phase systems offers two frequency components which in principle correspond to two different autocorrelation lengths. For this study the visibilities have been added as the feature size is much greater than the autocorrelation length and the images are not saturated, leading to a linear dependence for both autocorrelation lengths, and thus also for their addition. The comparison to the earlier study with the PMMA spheres [22] shows that the behavior of the dark-field over the range of autocorrelation lengths is similar, albeit the slope is slightly larger (12 %), also due to a different design energy [19].

The source size is a crucial parameter, important for the visibility of smaller fringe sizes. To estimate the source requirements, a system with a source grating placed at the position of the bending magnet can be imagined. In order to obtain high visibility, the source size should be smaller than half the period of the required source grating [25]. Smaller fringes require smaller source sizes. The simulations in Fig. 6 indicate that the visibility curve can be recovered for a source size of roughly 500 µm. The effect from the source size is overestimated due to the ideal simulation conditions. Placement errors and grating imperfections will lead to additional visibility reductions which shift the curves from Fig. 6 and Fig. 7 down to lower visibilities. Therefore, the estimated source size is an upper bound. For future experiments it would be beneficial to rotate the gratings by 90 ° as the source size in the vertical direction is significantly smaller than in the horizontal direction at 3rd generation synchrotrons. The green simulation values in Fig. 7 indicate the visibility potential specific setup parameters at optimal fringe orders can provide.

The CT reconstruction posed difficulties due to low statistics and noise. For the acquired data with a visibility of 0.13 and the number of phase steps used here, high temporal beam and sample stability were required for more than an hour. These problems could be solved in part through binning 2 horizontal by 25 vertical pixels over 5 angular projections to avoid saturation of the phase-stepping curve's visibility in the thickest parts of the lung. The best results were obtained for a min-max signal retrieval where only the minimum and the maximum of the phase-stepping curve were used to calculate the visibility as the signal retrieval algorithm failed to converge with Eq. 4. The reconstruction shows that the dark-field signal arises from the inflated lung tissue, but not the air spaces and the heart tissue. Small regions in the heart that showed some dark-field signal might be due to small air inclusions in the surface of the heart or the vertical binning of the data with modest positioning instability over the 1.5 h long acquisition. The origin should be investigated in future experiments. For improved acquisition protocols, the image quality could be improved by using more elaborate reconstruction algorithms such as shown by Guo et al. [43]

A dedicated system could be further optimized for higher visibilities, simpler mechanics, with envelope-gratings [49] (with the caveat of a fixed autocorrelation length), higher energies (if available at the beamline), and adjusted diffraction order separation. This would lead to simpler data analysis by simplifying the fringe to a single frequency and fewer required phase steps, improved dark-field sensitivity through smaller fringe periods, and/or better statistics. The proposed system optimization

to phase gratings of 2.2 µm provides improvements to the visibility and a reduced artifact from the diffraction orders. This could significantly reduce the dose compared to the shown measurements at 25 mGy entrance dose. All technologies required to manufacture these components exist already and thus provide feasible parameters to build the described system. If the source coherence is still problematic for the improved grating parameters or experiments with a lab-based X-ray tube are to be implemented, a dedicated source grating could be employed.

## Conclusion

Dark-field lung imaging is a promising diagnostic tool for the early detection of structural damage in the lungs. Early clinical trials have demonstrated the benefits of dark-field imaging; however, previous studies required analyzer gratings, which absorbed 50 % or more of the subject's X-ray radiation dose. This work outlines an approach that provides an equivalent absorption image to classical radiography systems, with the addition of a dark-field image.

Our work demonstrated the feasibility of dual-phase imaging at synchrotron facilities, able to cover a large autocorrelation space. However, for resolutions below those relevant for dark-field lung imaging, issues from multiple diffraction orders still need to be addressed.

The system lengths at synchrotron beamlines like SYRMEP allow for the measurement of relevant autocorrelation lengths without analyzer gratings by trading propagation distance for increased fringe period. The results of this first dark-field porcine lung study without analyzer gratings yielded the dark-field signal of porcine lungs as well as PMMA micro-spheres at autocorrelation lengths optimal for lung imaging at clinical doses, results which have not been reported before.

An interferometry system enabling full-scale dark-field lung imaging was detailed. Improvements to the interferometry system will lead to better results in terms of higher visibility, fewer phase steps for signal retrieval, and therefore, shorter imaging time and dose.

Dual-phase imaging offers a versatile tool to achieve a wide range of autocorrelation lengths, from a few nanometers up to the order of microns, making it an attractive option for measuring and characterizing the dark-field at synchrotron facilities. Future ring upgrades, which will reduce the source size of the systems, will further enhance the overall performance of dual-phase interferometers.

## Data Availability

The data and code of this study are publicly available on ETH Research Collection and GitHub.

### Ethical Agreement

The four porcine lungs utilized for this study were all acquired from a slaughterhouse as a side-product of the meat production chain. Therefore, no ethical agreement was required.

## References


1. Momtazmanesh, S. *et al.* Global burden of chronic respiratory diseases and risk factors, 1990–2019: an update from the Global Burden of Disease Study 2019. *eClinicalMedicine* **59**, 101936, DOI: 10.1016/j.eclinm.2023.101936 (2023).
2. Buist, A. S., Vollmer, W. M. & McBurnie, M. A. Worldwide burden of COPD in high- and low-income countries. Part I. The burden of obstructive lung disease (BOLD) initiative. *The international journal tuberculosis lung disease : official journal Int. Union against Tuberc. Lung Dis.* **12**, 703–8 (2008).
3. Schittny, J. C. How high resolution 3-dimensional imaging changes our understanding of postnatal lung development. *Histochem. Cell Biol.* **150**, 677–691, DOI: 10.1007/s00418-018-1749-7 (2018).
4. Lovric, G. *et al.* Automated computer-assisted quantitative analysis of intact murine lungs at the alveolar scale. *PLOS ONE* **12**, e0183979, DOI: 10.1371/journal.pone.0183979 (2017).
5. Lovric, G. *et al.* Tomographic in vivo microscopy for the study of lung physiology at the alveolar level. *Sci. Reports* **7**, 12545, DOI: 10.1038/s41598-017-12886-3 (2017).
6. Wagner, W. L. *et al.* Towards synchrotron phase-contrast lung imaging in patients – a proof-of-concept study on porcine lungs in a human-scale chest phantom. *J. Synchrotron Radiat.* **25**, 1827–1832, DOI: 10.1107/S1600577518013401 (2018).
7. Dullin, C., Wagner, W. L., Confalonieri, M. & Tromba, G. Pulmonary phase contrast CT imaging: a novel setup at the Italian synchrotron for the study of fresh lungs at human scale. *Eur. Respir. J.* **63**, 2301604, DOI: 10.1183/13993003.01604-2023 (2024).

8. Willer, K. *et al.* X-ray dark-field chest imaging for detection and quantification of emphysema in patients with chronic obstructive pulmonary disease: a diagnostic accuracy study. *The Lancet Digit. Heal.* **3**, e733–e744, DOI: 10.1016/S2589-7500(21)00146-1 (2021).

9. Viermetz, M. *et al.* Dark-field computed tomography reaches the human scale. *Proc. Natl. Acad. Sci.* **119**, e2118799119, DOI: 10.1073/pnas.2118799119 (2022).

10. Rawlik, M. *et al.* Increased dose efficiency of breast CT with grating interferometry. *Optica* **10**, 938, DOI: 10.1364/OPTICA.487795 (2023).

11. Partridge, T. *et al.* Enhanced detection of threat materials by dark-field x-ray imaging combined with deep neural networks. *Nat. Commun.* **13**, 4651, DOI: 10.1038/s41467-022-32402-0 (2022).

12. Organista, C. *et al.* Implementation of a dual-phase grating interferometer for multi-scale characterization of building materials by tunable dark-field imaging. *Sci. Reports* **14**, 384, DOI: 10.1038/s41598-023-50424-6 (2024).

13. Adams, S. J. *et al.* Lung cancer screening. *The Lancet* **401**, 390–408, DOI: 10.1016/S0140-6736(22)01694-4 (2023).

14. ICRP. The 2007 Recommendations of the International Commission on Radiological Protection. ICRP Publication 103. *Annals ICRP* **37** (2007).

15. Meuli, R., Hwu, Y., Je, J. & Margaritondo, G. Synchrotron radiation in radiology: radiology techniques based on synchrotron sources. *Eur. Radiol.* **14**, 1550–1560, DOI: 10.1007/s00330-004-2361-x (2004).

16. Pfeiffer, F. *et al.* Hard-X-ray dark-field imaging using a grating interferometer. *Nat. Mater.* **7**, 134–137, DOI: 10.1038/nmat2096 (2008).

17. Momose, A. Phase-contrast X-ray imaging based on interferometry. *J. Synchrotron Radiat.* **9**, 136–142, DOI: 10.1107/S0909049502003771 (2002).

18. Yashiro, W. & Momose, A. Effects of unresolvable edges in grating-based X-ray differential phase imaging. *Opt. Express* **23**, 9233, DOI: 10.1364/OE.23.009233 (2015).

19. Strobl, M. General solution for quantitative dark-field contrast imaging with grating interferometers. *Sci. Reports* **4**, 7243, DOI: 10.1038/srep07243 (2014).

20. Lynch, S. K. *et al.* Interpretation of dark-field contrast and particle-size selectivity in grating interferometers. *Appl. Opt.* **50**, 4310, DOI: 10.1364/AO.50.004310 (2011).

21. Gkoumas, S. *et al.* A generalized quantitative interpretation of dark-field contrast for highly concentrated microsphere suspensions. *Sci. Reports* **6**, 35259, DOI: 10.1038/srep35259 (2016).

22. Spindler, S. *et al.* The choice of an autocorrelation length in dark-field lung imaging. *Sci. Reports* **13**, 2731, DOI: 10.1038/s41598-023-29762-y (2023).

23. Gromann, L. B. *et al.* In-vivo X-ray Dark-Field Chest Radiography of a Pig. *Sci. Reports* **7**, 4807, DOI: 10.1038/s41598-017-05101-w (2017).

24. Kagias, M., Wang, Z., Jefimovs, K. & Stampanoni, M. Dual phase grating interferometer for tunable dark-field sensitivity. *Appl. Phys. Lett.* **110**, 014105, DOI: 10.1063/1.4973520 (2017).

25. Ge, Y. *et al.* Dual phase grating based X-ray differential phase contrast imaging with source grating: theory and validation. *Opt. Express* **28**, 9786, DOI: 10.1364/OE.381759 (2020).

26. Yang, J. *et al.* Analysis of period and visibility of dual phase grating interferometer. *Chin. Phys. B* **31**, 058701, DOI: 10.1088/1674-1056/ac3a60 (2022).

27. Judge, E. P. *et al.* Anatomy and Bronchoscopy of the Porcine Lung. A Model for Translational Respiratory Medicine. *Am. J. Respir. Cell Mol. Biol.* **51**, 334–343, DOI: 10.1165/rcmb.2013-0453TR (2014).

28. Longo, E. *et al.* SYRMEP beamline: state of the art, upgrades and future prospects. *The Eur. Phys. J. Plus* **139**, 880, DOI: 10.1140/epjp/s13360-024-05489-1 (2024).

29. Karantzoulis, E. *et al.* TOP-UP IMPLEMENTATION AND OPERATION AT ELETTRA. *Conf.Proc.C* (2010).

30. Dullin, C. *et al.* Multiscale biomedical imaging at the SYRMEP beamline of Elettra - Closing the gap between preclinical research and patient applications. *Phys. Open* **6**, 100050, DOI: 10.1016/j.physo.2020.100050 (2021).

31. Peiffer, C. *et al.* On the equivalence of the X-ray scattering retrieval with beam tracking and analyser-based imaging using a synchrotron source. *J. Phys. D: Appl. Phys.* **56**, 45LT02, DOI: 10.1088/1361-6463/acee8c (2023).

**32.** Dullin, C. *et al.* Novel setup for rapid phase contrast CT imaging of heavy and bulky specimens. *J. Synchrotron Radiat.* **30**, 650–654, DOI: 10.1107/S1600577523001649 (2023).

**33.** Li, K., Wojcik, M. & Jacobsen, C. Multislice does it all—calculating the performance of nanofocusing X-ray optics. *Opt. Express* **25**, 1831, DOI: 10.1364/OE.25.001831 (2017).

**34.** Munro, P. R. T. Rigorous multi-slice wave optical simulation of x-ray propagation in inhomogeneous space. *J. Opt. Soc. Am. A* **36**, 1197, DOI: 10.1364/JOSAA.36.001197 (2019).

**35.** Spindler, S. *et al.* Simulation framework for X-ray grating interferometry optimization. *Opt. Express* **33**, 1345, DOI: 10.1364/OE.543500 (2025).

**36.** Shi, Z., Jefimovs, K., Romano, L. & Stampanoni, M. Optimization of displacement Talbot lithography for fabrication of uniform high aspect ratio gratings. *Jpn. J. Appl. Phys.* **60**, SCCA01, DOI: 10.35848/1347-4065/abe202 (2021).

**37.** Tang, R. *et al.* Detailed analysis of the interference patterns measured in lab-based X-ray dual-phase grating interferometry through wave propagation simulation. *Opt. Express* **31**, 1677, DOI: 10.1364/OE.477964 (2023).

**38.** Yan, A., Wu, X. & Liu, H. Predicting fringe visibility in dual-phase grating interferometry with polychromatic X-ray sources. *J. X-Ray Sci. Technol. Clin. Appl. Diagn. Ther.* **28**, 1055–1067, DOI: 10.3233/XST-200726 (2020).

**39.** Wang, Z. *et al.* Non-invasive classification of microcalcifications with phase-contrast X-ray mammography. *Nat. Commun.* **5**, 3797, DOI: 10.1038/ncomms4797 (2014).

**40.** Petrache, I. & Serban, K. Emphysema. In *Pathobiology of Human Disease*, 2609–2624, DOI: 10.1016/B978-0-12-386456-7.05305-3 (Elsevier, 2014).

**41.** van Aarle, W. *et al.* The ASTRA Toolbox: A platform for advanced algorithm development in electron tomography. *Ultramicroscopy* **157**, 35–47, DOI: 10.1016/j.ultramic.2015.05.002 (2015).

**42.** van Aarle, W. *et al.* Fast and flexible X-ray tomography using the ASTRA toolbox. *Opt. Express* **24**, 25129, DOI: 10.1364/OE.24.025129 (2016).

**43.** Guo, P. *et al.* Analytical Reconstruction of Human-Scale Dark-Field CT. *IEEE Transactions on Med. Imaging* 1–1, DOI: 10.1109/TMI.2025.3592849 (2025).

**44.** Münch, B., Trtik, P., Marone, F. & Stampanoni, M. Stripe and ring artifact removal with combined wavelet—Fourier filtering. *Opt. Express* **17**, 8567, DOI: 10.1364/OE.17.008567 (2009).

**45.** Karantzoulis, E. & Barletta, W. Aspects of the Elettra 2.0 design. *Nucl. Instruments Methods Phys. Res. Sect. A: Accel. Spectrometers, Detect. Assoc. Equip.* **927**, 70–80, DOI: 10.1016/j.nima.2019.01.044 (2019).

**46.** Pandeshwar, A., Kagias, M., Wang, Z. & Stampanoni, M. Modeling of beam hardening effects in a dual-phase X-ray grating interferometer for quantitative dark-field imaging. *Opt. Express* **28**, 19187, DOI: 10.1364/OE.395237 (2020).

**47.** De Marco, F. *et al.* X-Ray Dark-Field Signal Reduction Due to Hardening of the Visibility Spectrum. *IEEE Transactions on Med. Imaging* **43**, 1422–1433, DOI: 10.1109/TMI.2023.3337994 (2024).

**48.** Blaskovic, S. *et al.* Airspace Diameter Map—A Quantitative Measurement of All Pulmonary Airspaces to Characterize Structural Lung Diseases. *Cells* **12**, 2375, DOI: 10.3390/cells12192375 (2023).

**49.** Pandeshwar, A., Kagias, M., Shi, Z. & Stampanoni, M. Envelope modulated x-ray grating interferometry. *Appl. Phys. Lett.* **120**, 193701, DOI: 10.1063/5.0087940 (2022).


## Acknowledgements


The authors thank Gordan Mikuljan for his assistance throughout the design process of the grating holder. Certain commercial equipment, instruments, or materials are identified in this paper in order to specify the experimental procedure adequately. Such identification is not intended to imply recommendation or endorsement by NIST, nor is it intended to imply that the materials or equipment identified are necessarily the best available for the purpose.


## Author Contributions

G.T. and M.S. conceptualized the project, S.S., C.D., A.C., E.L., N.S., M.R., G.T. and M.S. planned the beamtime, S.S., A.P., C.O., M.Z., G.Lo., G.La., C.D., A.C., E.L., N.S., L.D. and G.T. conducted the experiments, L.R., K.J., D.J. fabricated the gratings, S.S., A.P., C.O., M.Z., G.Lo. did the data analysis, S.S. performed the simulations, S.S. took the lead in writing the manuscript. All authors reviewed the manuscript and provided feedback.

## Funding

This work was funded by SwissLOS Lottery Fund of Kanton Aargau, SNF R'Equip 189662 (SiDRY), SNF R'Equip 177036 (DLT), PHRT-Pioneer Project Nr. 2021-612 CLARINET, SNF Sinergia Grant Nr. CRSII5, PHRT-TT Project Nr. 2022-572 INTIMACY and Promedica Stiftung Chur – Project Nr. 1572.

## Additional Information

The authors declare no competing interests.